ADVANCED FUNCTIONAL MATERIALS
www.afm-journal.de

Quantifying Spin Defect Density in hBN via Raman and Photoluminescence Analysis

Atanu Patra, Paul Konrad, Andreas Sperlich, Timur Biktagirov, Wolf Gero Schmidt, Lesley Spencer, Igor Aharonovich, Sven Höfling, and Vladimir Dyakonov**

Negatively charged boron vacancies (V_B^-) in hexagonal boron nitride (hBN) are emerging as promising solid-state spin qubits due to their optical accessibility, structural simplicity, and compatibility with photonic platforms. However, quantifying the density of such defects in thin hBN flakes has remained elusive, limiting progress in device integration and reproducibility. Here, an all-optical method is presented to quantify V_B^- defect density in hBN by correlating Raman and photoluminescence (PL) signatures with irradiation fluence. Two defect-induced Raman modes, D1 and D2, are identified and assigned them to vibrational modes of V_B^- using polarization-resolved Raman measurements and density functional theory (DFT) calculations. By adapting a numerical model originally developed for graphene, an empirical relationship linking Raman (D1, E_{2g}) and PL intensities is established to absolute defect densities. This method is universally applicable across various irradiation types and uniquely suited for thin flakes, where conventional techniques fail. The approach enables accurate, direct, and non-destructive quantification of spin defect densities down to 10^{15} defects/cm^3, offering a powerful tool for optimizing and benchmarking hBN for quantum optical applications.

1. Introduction

Hexagonal boron nitride (hBN) has become an indispensable part of device fabrication using van der Waals (vdW) materials, serving both as an encapsulation and an insulator due to its large band gap of 6 eV.[1] Furthermore, identification of optically active negatively charged boron vacancy spin defects (V_B^-) in hBN by Gottscholl et. al.[2] has garnered significant interest in the field of quantum sensing as V_B^- offers a robust platform for quantum technologies that can operate at room temperature. Specifically, it has been shown that V_B^- centers are highly sensitive to their environment,[2–5] making them ideal quantum sensors for magnetic fields,[6,7] temperature, and pressure.[8] In general, due to their reduced dimensionality, spin defects in 2D van der Waals (vdW) materials offer unique advantages over their counterparts in 3D systems, such as nitrogen-vacancy centers in diamond and spin defects in silicon carbide. In the case of hBN, this 2D nature allows for the creation of stable spin defects near the sample surface, significantly enhancing the precision of quantum sensing.[2,4] Moreover, the atomic thinness, stability, and chemical inertness of hBN provide a scalable platform for integrating spin defects into various hybrid photonic devices[9–11] and even for use in studying complex charge dynamics in aqueous environments.[12,13] Such applications of hBN largely depend on the precise control and distribution of spin defects in it. Although defect generation can be achieved by various types of

A. Patra, S. Höfling
Lehrstuhl für Technische Physik
Julius-Maximilians-Universität Würzburg
Am Hubland, Würzburg 97074, Deutschland
E-mail: atanu.patra@uni-wuerzburg.de

P. Konrad, A. Sperlich, V. Dyakonov
Experimental Physics VI
Julius-Maximilians-Universität Würzburg
Am Hubland, Würzburg 97074, Deutschland
E-mail: vladimir.dyakonov@uni-wuerzburg.de

The ORCID identification number(s) for the author(s) of this article can be found under https://doi.org/10.1002/adfm.202517851

DOI: 10.1002/adfm.202517851

A. Sperlich, S. Höfling, V. Dyakonov
Physikalisches Institut and Würzburg-Dresden Cluster of Excellence ct.qmat
Deutschland

T. Biktagirov, W. G. Schmidt
Department Physik
Universität Paderborn
Warburger Str. 100, Paderborn 33098, Deutschland

L. Spencer, I. Aharonovich
School of Mathematical and Physical Sciences
University of Technology Sydney
Ultimo, NSW 2007, Australia

I. Aharonovich
ARC Centre of Excellence for Transformative Meta-Optical Systems
University of Technology Sydney
Ultimo, NSW 2007, Australia

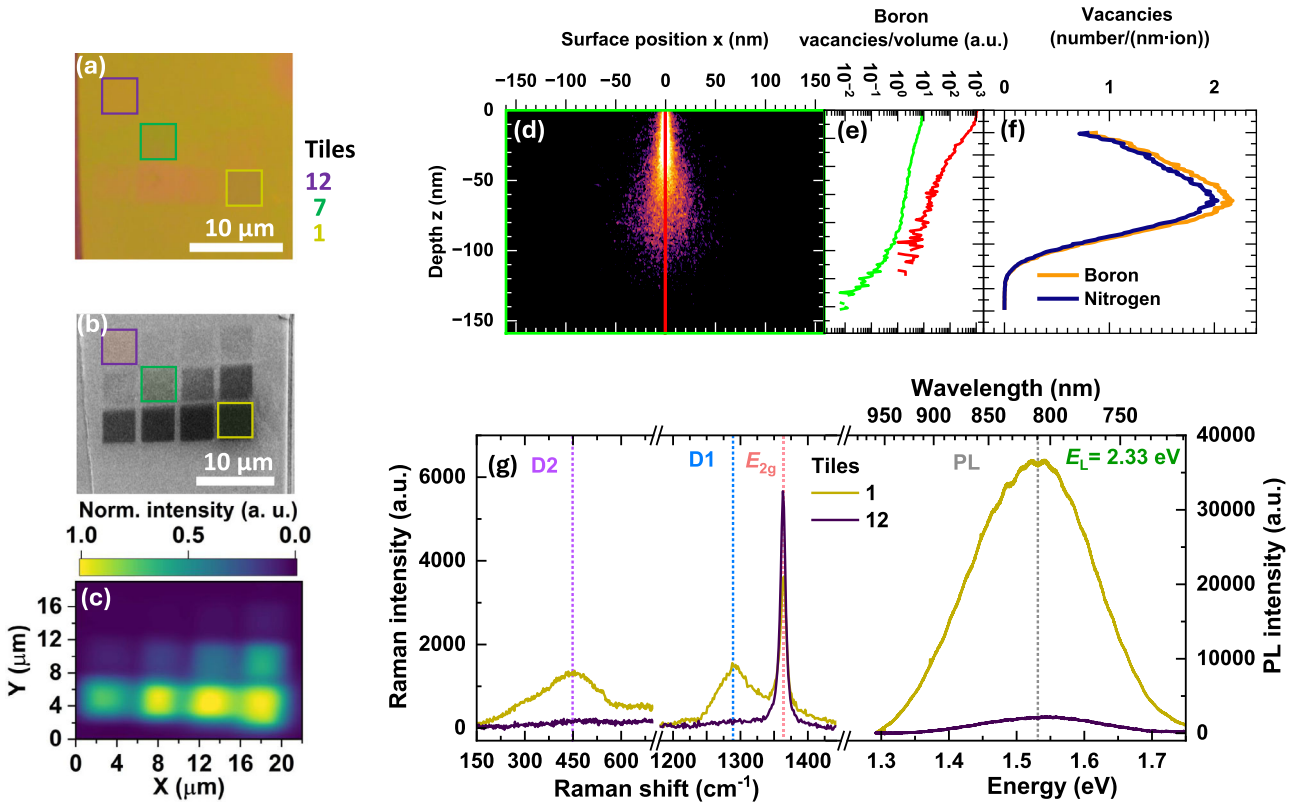

Figure 1. a) Optical b) SEM and c) integrated PL images of irradiated hBN (Sample-1). The areas are labeled as Tiles 1-12, irradiated with decreasing ion fluence. Tile-1 (yellow) was irradiated with the highest fluence (11.5 ions/nm^2) and Tile-12 (violet) with the lowest (0.01 ions/nm^2). For PL maps, spectra have been recorded point-by-point and the spectra have been integrated from 1.37 eV to 1.65 eV. d) Simulated boron vacancy density created by a focused ion beam using the software SRIM. The depiction represents a cross section in the x-z plane where the x-y plane is parallel to the sample surface. The density is shown on a logarithmic color scale. e) Vertical line profiles for the red line shown in (d), while the green line is averaged over the x-dimension (green box around (d)). f) Depth distribution of the vacancy yield per ion distinguished by target atom. The data is the sum of every vacancy created at a certain depth regardless of the x or y position. g) Characteristic spectra of the Raman modes D2, D1, E_{2g} and PL for Tiles 1 and 12 with a laser excitation energy of E_L = 2.33 eV (532 nm).

irradiaiton like focused ion beams,[14] neutrons,[2,15] laser writing[16] and electrons,[17] the absolute spin-defect density is greatly dependent on irradiation parameters and sample properties.

The emitted photoluminescence (PL) then depends on the type of defects present in the system.[18] The PL of V_B^- has a broad, featureless spectrum in the near infrared ≈850 nm. So far, the zero phonon line has not been resolved yet but was estimated to be at 773 nm.[10] The electronic dipole moment linked to a defect influences its PL. Furthermore, we also investigate the defect-related vibrational modes and hence correlation to defect PL. In this regard, Raman spectroscopy is a valuable tool in the understanding of the vibrational modes in 2D materials. In particular, Raman spectroscopy of graphene has been instrumental in the study of its crystal structure and defects. Both, graphene and hBN have a hexagonal crystal structure with D_{6h} and D_{3h} point-group symmetry respectively. The main difference is the unit cell composition. Graphene consists of carbon atoms, whereas hBN contains boron and nitrogen, thus reducing symmetry. The characteristic Raman peak in graphene is at 1585 cm^{-1}, which is a plane high frequency E_{2g} and, additionally, a defect activated mode, D peak is at 1350 cm^{-1}.[19,20] Several works have shown the quantification of the crystal size (L_a) in graphene, and thereby the defect-density from the relative contribution of the E_{2g} and D peak in nanographites,[19,21–24] amorphous carbons, carbon nanotubes and graphene.[25,26] Similar to graphene, recent studies have identified[15,27–30] a defect-related Raman peak in hBN. Vibrational modes of several prominent defects in hBN have also been addressed theoretically.[31] Although methods such as electron paramagnetic resonance (EPR)[8] and single defect counting by PL mapping exist for an estimation of emitter density, they are hardly applicable to the low absolute number of defects found in thin flakes that also have a low photon count rate. Furthermore, a standardized protocol for direct determination of spin-defect density solely from spectral data could not be established yet.

In this work, we have investigated two emerging Raman modes, labeled as D1 and D2 following the convention from the graphene literature, alongside the well-established E_{2g} mode in hBN. We find that these newly identified Raman modes are associated with V_B^- defects, which emit a distinctive PL signal in the near infrared under laser excitation, and support this assignment using density functional theory (DFT) calculations. Both, D1 and PL intensities, increase with laser excitation energy (E_L), providing insights into the optical absorption and intrinsic properties of

V_B^- spin defects. Polarization-dependent Raman measurements were employed to understand the symmetry and origin of these modes. We generated V_B^- defects by focused nitrogen ion beam irradiation in hBN with varying fluence and find that the intensities of Raman modes and PL signal correlate with the fluence, and hence with defect density. By analyzing the dependence of area of the D1 and E_{2g} Raman modes along with PL, we developed a method to directly quantify spin density as a function of relative Raman and PL intensities alone, which is crucial for both fundamental research and practical applications.

2. Results

2.1. Correlation of Raman and PL signals with spin defects

Bulk hBN was dry-transferred onto two substrates: SiO_2/Si (referred to as Sample-1) and a Au/Cu gold-coated copper stripline (referred to as Sample-2). V_B^- defects were introduced by nitrogen irradiation at increasing fluences in a tile pattern (4 μm × 4 μm tiles). Details are provided in the Supporting Information, refer to Tables S1 and S2 (Supporting Information). Optical and scanning electron microscopy (SEM) images of Sample-1 are shown in **Figure 1**a,b, respectively. The color contrast of the array of tiles displays the variation in fluence. The PL map in Figure 1c, obtained from integrated and normalized PL spectra, directly mirrors the irradiation pattern observed in the optical and SEM images.

The irradiation impact of the nitrogenfocused ion beam was simulated using the software SRIM (The Stopping and Range of Ions in Matter) and is shown in Figure 1d–f. For the calculations, monolayer collision steps and a full collision report were calculated for ≈10^4 ions and analyzed afterward (for more details see Supporting Information). A lateral x-z cross section of the ion-induced damage plume is shown in panel (d) where the color of each pixel represents the amount of boron vacancies created per 1 nm^3 on a logarithmic scale. The x-y plane of the simulation is parallel to the sample surface and z is the depth below the surface. The profile along the red line in (d) is shown in sub panel (e). The green profile is additionally averaged over the x-axis. When we take also the y-dimension into account, we get a comprehensive view of the vacancies created in a certain depth. The data shown in panel (f) represent the vacancy yield per ion as a function of depth, obtained by dividing the average vacancies created at depth z by the number of ions used in the simulation. As can be seen, the defects are all created within ≈100 nm depth of the surface with approximately equal share of boron and nitrogen vacancies present. While this is a valid result, SRIM is not suitable to predict absolute defect densities as it treats damage cascades independently and does not consider secondary effects such as defect annealing, charge state, interstitials, etc.

Figure 1g shows the Raman and PL spectra measured at two tiles on Sample-2: Tile-1 (yellow) corresponds to the highest irradiation fluence, while Tile-12 (violet) represents the lowest. The whole spectrum was recorded in a single measurement with excitaion laser energy E_L = 2.33 eV (λ_L = 532 nm). The Raman spectra are shown in cm^{-1}, and the PL spectra in electronvolts (eV) for clarity. We note that two samples were used in this study: Sample-1 is the main analysis sample, but the Si background partially overlaps with the D2 Raman mode (see Figure S1, Supporting Information). Sample-2 reduces this background, allowing clearer identification of D2.

The most prominent mode of the Raman spectrum is at ≈1365 cm^{-1}, which corresponds to the E_{2g} phonon at the Brillouin zone center. Notably, the peak position provides information about the nature of present isotopes due to the mass difference between ^{10}B and ^{11}B isotopes.[32,33] hBN with a single boron isotope retrieved from either ^{10}B-or ^{11}B-enriched hBN show the E_{2g} mode at 1358(1) cm^{-1}, respectively. In pyrolytic BN (pBN), it appears at 1367(1) cm^{-1}.[15] The next prominent features in the Raman spectrum are observed at ≈1290 cm^{-1} and 450 cm^{-1}, labeled as D1 and D2 respectively in Figure 1g. These peaks are associated with V_B^- defects in hBN and pBN,[15,27,28,31] and are notably absent for carbon-based defects in hBN.[34,35] The absence of transverse optical Raman modes associated with cubic-BN (cBN) at 1055 cm^{-1} excludes the possibility of hBN-to cBN transition.[36,37]

The characteristic and broad PL signature of V_B^- defects is observed at ≈ 1.53 eV (810 nm) at room temperature. In contrast to Raman modes, PL does not exhibit isotope dependence, as reported previously.[5,15,38] **Table 1** summarizes the Raman and PL peaks related to various defects in hBN, as observed in this study and as reported in the literature.[15,27,28,34,39,40] The peak position of the D1 mode in hBN is independent (non-dispersive) of the used laser energy E_L, unlike the D mode in graphene.[20] We corroborate this finding for three different E_L as shown in Figure S2 (Supporting Information). The different dispersion relation in comparison to graphene is to be expected as we are not dealing with a semi-metal with a Dirac-cone band structure, but with an insulator.

2.2. Polarization-Dependence

To gain deeper insight into the structure of of the Raman modes, specially D1 and D2 modes we conducted linear polarization-dependent Raman measurements at Tile-4 (3.2 ions nm^{-2}) of Sample-2, as shown in **Figure 2**. The polarization direction of the incident laser light is varied using a half wave plate ($\lambda/2$) which is introduced into the optical path of incident light, along with an analyzer in the scattered path. For a fixed incident laser polarization, the analyzer confines the scattered light either in horizontal or in vertical configuration. Figure 2 presents data for parallel polarization of excitation and emission. The orthogonal configuration exhibits similar behavior with reversed features as the $\lambda/2$ plate rotates relative to the sample axis with an angle θ (see Figure S3, Supporting Information). By continuously varying the $\lambda/2$ plate, we can go from a $Z(XX)\bar{Z}$ to $Z(YX)\bar{Z}$ configuration, corresponding to parallel (∥) and perpendicular (⊥) polarization measurements, respectively. This is illustrated in the inset of Figure 2a. In this notation, the first and fourth term represent the direction of incident and scattered light, respectively. While the second and third terms denote the polarization in the direction of the incident and scattered light, respectively. In Figure 2a, spectra for ∥ and ⊥ polarizations are shown in red and blue, respectively. In Figure 2b,c, contour plots that capture the full polarization dependence of the Raman modes and PL are shown. These plots reveal that the intensities of the PL, E_{2g}, and D1 modes remain constant against the rotation of the $\lambda/2$ plate. In contrast, the D2

Table 1. Summarizing the Raman and PL modes corresponding to different defects in hBN, as identified in the present study (★) and reported earlier.[15,27,28,34,39,40]

Type of defect	Process	Raman modes [cm^{-1}]			PL mode [eV]
		D2	D1	E_{2g}	
	Nitrogen irradiation ★	450	1290	1365	1.53 (810 nm)
	Neutron transmutation in ^{10}B[15]	450	1296	1367.2	1.55 (800 nm)
V_B^-	^{12}C, ^{20}Ne, ^{69}Ga irradiation[27]	–	1290	1357	1.99 (620 nm) & 1.53 (810 nm)
	Helium irradiation[28,29]	448	1295	1367	1.5 (830 nm)
$V_BC_N^-$	Carbon-doped[34,39,40]	–	–	1366	2.11 (585 nm)

mode demonstrates a pronounced dependence on it, highlighting its distinct behavior compared to the other modes. A high-resolution measurement using a 1800 lines mm^{-1} grating reveals that the D2 mode for ∥ polarization is comprised of two components, denoted as D2a and D2b. In contrast, for ⊥-polarization, only a single mode is observed, as presented in Figure 2d. The intensities of different peaks from the contour plot in Figure 2b,c, normalized with respect to their $Z(XX)\bar{Z}$ values, are depicted in Figure 2e. This illustrates that only the D2 modes (D2a and D2b) follow the $\cos^2\theta$ dependence, as indicated by the solid orange line in Figure 2f.

The intensity of Raman modes is expressed as $I_R \propto \left|e_{in}^T \cdot \hat{R} \cdot e_{out}\right|^2$, where $\hat{R}$ is the Raman tensor.[41] The interaction between the in-plane polarization of the incident light and atomic vibrations alters the polarizability and the Raman tensor, which is reflected in the Raman signal. Consequently, the intensity of the E_{2g} mode exhibits an isotropic behavior with respect to θ, with an expected response of $I_R \propto$ constant. Such isotropic variation of E_{2g} is reported for basal plane measurement in graphene[42] and transition metal dichalcogenide (TMDC) materials.[43,44]

It is noteworthy that we are dealing with the V_B^- point defects with zero-field splitting parameter $D \approx 3.5$ GHz.[2] The positive value of D describes that the electronic distribution around the defect center has an oblate shape. We believe that this oblate shape influences the electronic polarizability, which

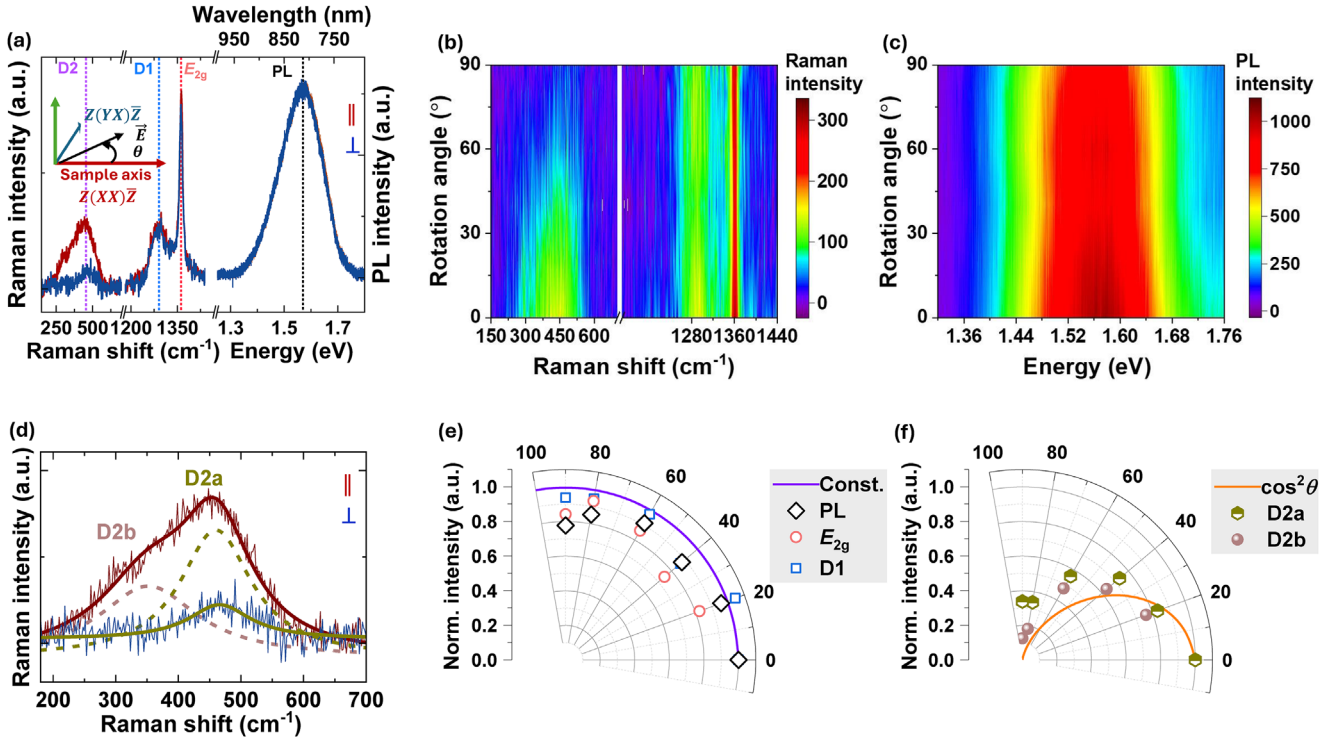

Figure 2. Linear polarization-dependent Raman modes: a) Spectra corresponding to $Z(XX)\bar{Z}$ and $Z(YX)\bar{Z}$, are shown in red and blue, respectively. The color contour plots present the variation of Raman b) and PL signals c) with respect to incident light polarization direction. d) Lorentzian fitting of the D2 mode for two polarization configurations. For ∥ polarization, the D2 peak is resolved into two sub-modes, D2a and D2b, appearing at ≈ 459 and 352 cm^{-1} with width $\Gamma \approx 138$ and 191 cm^{-1}, respectively. In contrast, for ⊥-polarization, D2b is not detected, and D2a appears with reduced intensity at 465 cm^{-1} with $\Gamma \approx 120$ cm^{-1}. e,f) Polar plots of all Raman modes and the PL signal, normalized to their $Z(XX)\bar{Z}$ values. (e) Representing the isotropic behavior of PL, E_{2g}, and D_1. (f) $\cos^2\theta$ dependence of D2a and D2b.

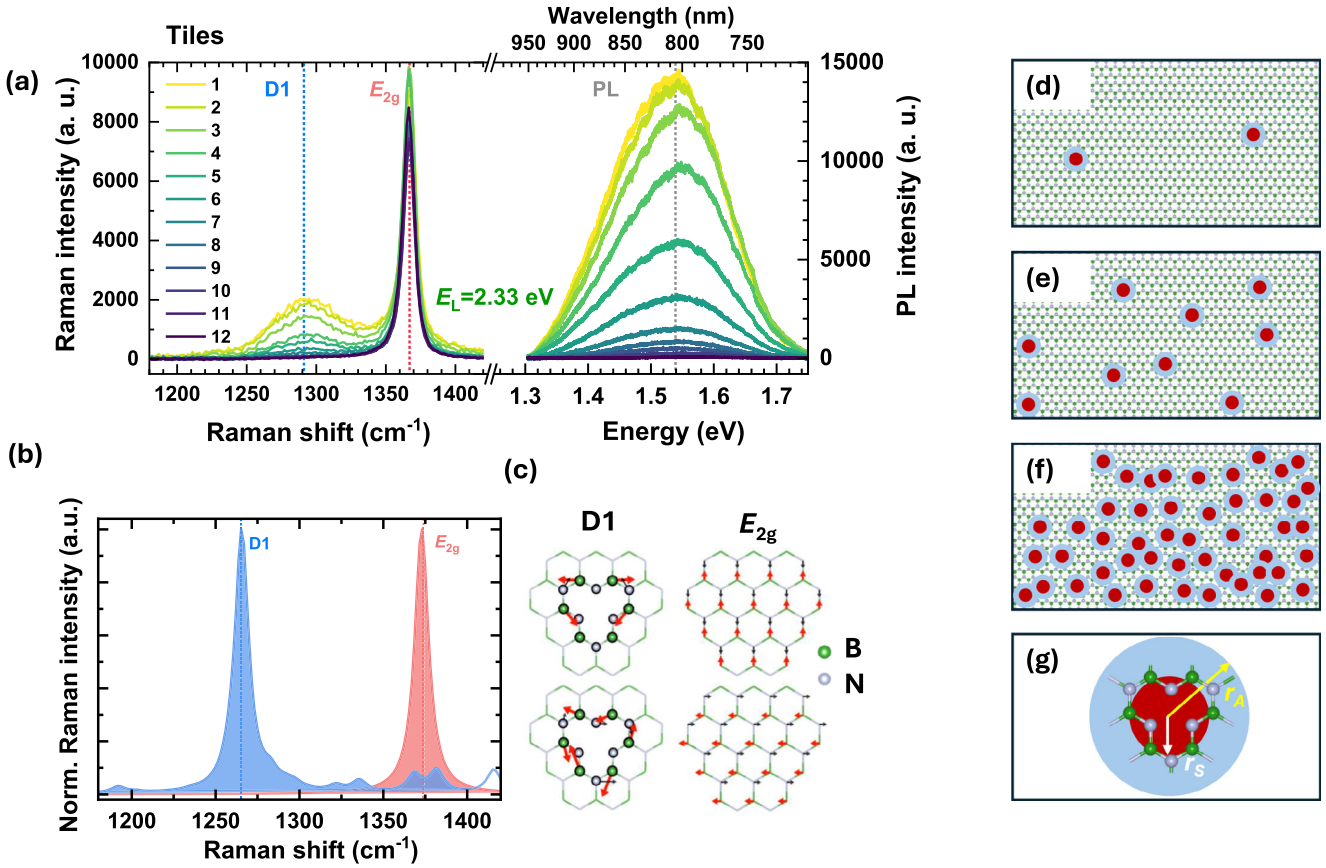

Figure 3. a) Characteristic Raman and PL spectra recorded at different tiles, as shown in Figure 1a,b. b) Calculated Raman spectrum and c) Schematic diagram of atomic vibrations responsible for different Raman modes. d–f) Schematic illustrations of defect densities for each irradiation fluence are presented in panels, adapted from.[25] As the defect density increases, the overlap becomes more pronounced, adversely affecting both the Raman and PL signals. g) The red region represents the area directly impacted by ion collisions, while the light blue region indicates the extent to which the ion impacts remain visible.

contributes to the observation of additional Raman modes. Further analysis of the Raman intensity with θ demonstrates a similar isotropic variation of E_{2g} and D1 modes in Figure 2e. This suggests that similar to the E_{2g}-mode, in-plane atomic vibrations around the defect are associated with the D1 mode, as presented in schematic diagram **Figure** 3c. However, for atomic vibrations out of the basal plane, the Raman intensity follows $I_R \propto a \cos^2 \theta$, as observed in TMDCs.[43,45] A similar θ dependence is observed for both D2 modes in this study, confirming that their atomic vibrations are orthogonal to the E_{2g} and D1 modes, as illustrated in Figure 2f.

Furthermore, we studied the dependence on laser excitation energy (E_L) of 2.62 eV (473 nm), 2.33 eV (532 nm), and 1.96 eV (633 nm) and find that PL and Raman spectra reveal a clear dependence as shown for Sample-2 in Figure S4 (Supporting Information). PL intensity peaks near the absorption maximum at $E_L \approx 2.6$ eV and remains strong even at 2.33 eV, which might be due to enhanced ionization of neutral boron vacancies (V_B^0) into their optically active charged state V_B^-.[46] We find that E_{2g} follows expected trends with excitation energy for a Raman mode. In contrast to that, the D1 mode mirrors the PL response, suggesting a shared origin linked to defect density and photo-induced ionization effects.

2.3. Fluence-Dependence

Figure 3a shows the PL and Raman modes of Sample-1 at different tiles corresponding to varying irradiation fluences, as indicated in the images in Figure 1. An increase in irradiation fluence is expected to generate more spin defects.[14] Consistent with this expectation, we observe an increase in intensity of the defect-related PL and D1 Raman modes with increasing irradiation fluence in Figure 3a, while the intensity of E_{2g} remains almost constant within the experimental error. The observed similarity in the changes in D1 and PL signals indicates a possible direct correlation between the Raman and PL responses.

In addition to the observed intensity changes, the Raman line width Γ of the E_{2g} -mode provides information about the crystal structure. Specifically, the lower Γ value for the E_{2g}-mode at Tile-12, compared to Tile-1 shown in Figure S5 (Supporting Information), indicates that the crystallinity of hBN is better preserved for the low irradiation in Tile-12. To further illustrate this, the variations in Γ over the irradiation fluence for the E_{2g} and D1 modes, as well as for the PL width, are presented in Figure S5 (Supporting Information). These data sets highlight that Raman and PL width correlate with the irradiation fluence, reinforcing the impact of irradiation on the structural integrity of hBN.

To associate the Raman peaks in Figures 1g and 3a with specific vibrational modes of the boron vacancy, we carried out DFT calculations using a supercell model with periodic boundary conditions. While the vibrational eigenmodes of defects in hBN, including the boron vacancy, have been previously studied with DFT,[31] the mere presence of such modes does not guarantee their appearance in the Raman spectrum. Here, to calculate the Raman activities of the vibrational modes of V_B^-, we considered a non-resonant Raman process, assuming an average over the polarizations of incident and scattered light.[47] The Raman scattering efficiency was approximated by non-spin-polarized calculations, while ensuring that the calculated vibrational modes are consistent with those of the triplet state. As shown in red in Figure 3b, the frequency of the E_{2g} mode obtained from our calculations for a pristine hBN monolayer (8 × 8 unit cells, 128 atoms) aligns well with the experiment. When V_B^- is introduced into the supercell, the calculated Raman spectra reveal prominent defect-induced Raman-active modes in the frequency regions corresponding to the experimental D1 and D2 peaks (Figure 3b; Figure S6, Supporting Information).

The double-degenerate vibrational mode at 1265 cm^{-1} (at the D1 peak) exhibits a large amplitude and is strongly localized near the defect, identifying it as a typical "local mode".[48] Its vibrational pattern is shown in Figure 3c. The calculated inverse participation ratio (IPR), used to quantify the degree of localization, is 11.6, indicating that this mode is predominantly localized on only ≈12 atoms in the supercell.[49] This explains why its frequency is independent of the supercell size (cf. Figure S7, Supporting Information) and is largely resilient to variations in the local defect concentration within the sample. The quasi-local nature of the vibrational mode D2 is explained in detail in Figures S6 and S7 (Supporting Information).

2.4. Phenomenological Model

In the determination of defect density, refs. [25, 26] emphasize the importance of considering the distance between point like defects. These studies propose an empirical model based on the intensity ratio of D and E_{2g} Raman modes in graphene. Figure 3d–f shows schematics of the crystal structure containing defects, adapted from ref. [25]. The phenomenological model is derived by solving geometrical rate equations considering the evolution of a structurally deformed region (S-, shown in red in Figure 3g) expanding up to a radius r_S and adjacent activated region (A-, shown in light blue in Figure 3g) expanding up to r_A with irradiation fluence. Beyond r_S, the lattice structure is preserved. Nevertheless, the proximity to defects leads to a mixing of Bloch states near high-symmetry points up to distance r_A, breaking selection rules and resulting in the emergence of D-Raman modes. The derived equation for the ratio of the Raman intensities is given by:[25]

$$\frac{I_D}{I_{E_{2g}}} = C_A \frac{r_A^2 - r_S^2}{r_A^2 - 2r_S^2}\left[\exp\left(-\frac{\pi r_S^2}{L_D^2}\right) - \exp\left(-\frac{\pi\left(r_A^2 - r_S^2\right)}{L_D^2}\right)\right] + C_S\left[1 - \exp\left(-\frac{\pi r_S^2}{L_D^2}\right)\right] \quad (1)$$

The distance between defects is considered by the characteristic length L_D. C_A and C_S are scaling factors for activation and structural deformation, respectively.

We fitted all Raman and PL spectra and used the areas for further analysis as shown in Figure S4 (Supporting Information). In our further analysis, we exclude the delocalized D2 mode due to its spectral overlap with silicon modes and its weak intensity. The areas of D1 (A_{D1}), E_{2g} ($A_{E_{2g}}$), and PL (A_{PL}) are are plotted as a function of irradiation fluence in Figure S9 (Supporting Information) for all three E_L. Notably, the intensity of A_{PL} is approximately two orders of magnitude higher than A_{D1}. However, when normalizing these variations relative to their maximum values, as shown in **Figure 4a**, a correlation between A_{PL} and A_{D1} becomes apparent – i.e. the relative responses of A_{PL} and A_{D1} to ion fluence changes are similar. We therefore introduce a single metric $(\frac{A_{D1}}{A_{E_{2g}}} + \frac{A_{PL}}{A_{E_{2g}}})$ to make use of both fluence-dependent V_B^- signatures normalized to the E_{2g} reference. Still, using only $\frac{A_{D1}}{A_{E_{2g}}}$ or $\frac{A_{PL}}{A_{E_{2g}}}$ is sufficient for this analysis – however with reduced SNR. While maintaining the same physical meaning of r_S, r_A and L_D, we adjust the scaling factors for activation (C'_A) and structural deformation (C'_S) to apply to both A_D and A_{PL}. Consequently, Equation (1) is modified to:

$$\frac{A_{D1} + A_{PL}}{A_{E_{2g}}} = C'_A \frac{r_A^2 - r_S^2}{r_A^2 - 2r_S^2}\left[\exp\left(-\frac{\pi r_S^2}{L_D^2}\right) - \exp\left(-\frac{\pi\left(r_A^2 - r_S^2\right)}{L_D^2}\right)\right] + C'_S\left[1 - \exp\left(-\frac{\pi r_S^2}{L_D^2}\right)\right] \quad (2)$$

The PL is solely associated with the spin carrying V_B^- defect, as follows from optically detected magnetic resonance.[2,5] According to our previous discussion, it follows that D1 can also be associated with the spin defect. Hence, we assume that the characteristic length LD that we extract represents the spacing between spin-defect. We can further relate L_D to the irradiation fluence through $L_D = \frac{\alpha}{\text{Fluence}^\beta}$, where α is a proportionality factor and β is a fluence-dependence exponent. We then fit Equation (2) to the data in Figure 4b for all three E_L. r_A, α, and β are set as global parameters shared across all three E_L, while C'_A and C'_S are specific to each individual E_L, as shown in Figure S10. The fitting yields $\alpha = 4.27 \pm 0.93$, $\beta = 0.6 \pm 0.02$, and $r_A = 2.42 \pm 0.43$ nm, with $r_S = 1.0$ nm (as determined for structural disorder.[25]) For E_L = 1.33 eV, only *data* points up to Tile-8 are included in the analysis, as both PL and Raman intensities decrease substantially beyond this point (see wavelength-dependence of Sample-2 in Figure S4). In graphene the Raman relaxation length is reported to be ≈ 2–4 nm.[25,26] We find r_A-$r_S \approx 1.4$ nm, which suggests a shorter Raman relaxation length of the D1 mode in hBN. Following from this analysis, we now calculate the volume spin density, $n_D = \frac{10^{21}}{(4/3)\pi L_D^3}$ in cm^{-3}, as illustrated in Figure 4c, with the shaded area depicting the potential error associated with the fitting. Furthermore, the estimated spin defect density adheres a power law with respect to irradiation fluence $C \cdot D^\gamma$, as shown by the solid line in the figure, with an exponent of $\gamma = 1.8 \pm 0.01$. From this graph, the spin density can be read out directly as function of 30 keV nitrogen irradiation fluence.

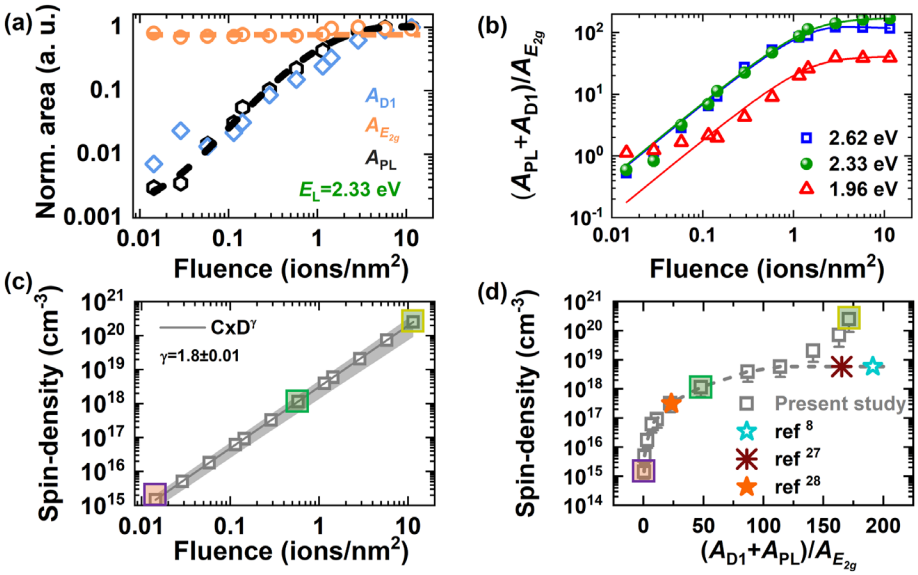

Figure 4. a) Dependence of integrated area A under curve for D1, E_{2g} Raman modes and PL at E_L = 2.33 eV on the irradiation fluence. Dotted traces are guides to the eye. b) Data points represent $(A_{D1} + A_{PL})/A_{E_{2g}}$, and the solid traces are calculated following Equation (2) for three E_L values. c) The calculated spin density using Equation (2). The shaded area represents the error associated with the fitting. The solid line is a fit of $C \cdot D^{\gamma}$ with $\gamma = 1.8 \pm 0.01$, representing the power law dependence of the spin-defect density on the irradiation fluence. The colored boxes mark the values for the corresponding tiles in Figure 1. d) The plot illustrates the direct estimation of spin defect density from the ratio $(A_{D1} + A_{PL})/A_{E_{2g}}$ in uncharacterized systems based on spectral response. The dashed line is a guide to the eye. The values $(A_{D1} + A_{PL})/A_{E_{2g}}$ ≈191,[8] ≈165[27] and ≈20,[28] calculated from spectral response data in these references, following the described method are marked by different asterisks.

Finally, to enable a straightforward estimation of spin-defect density by a single spectral measurement *independent* of irradiation type, we plot the spin-defect density against the ratio $(A_{D1} + A_{PL})/A_{E_{2g}}$ in Figure 4d. We observe that for a range of four orders of magnitude up to a density of 10^{19} / cm^3 the model accurately describes the dependence on the extracted Raman and PL intensities. Therefore, by measuring Raman and PL signatures of V_B^-, with this graph alone, it is possible to determine the spin defect density. If experimentally either D1 or PL are not accessible, this analysis is still valid by using only the ratio of $A_{D1}/A_{E_{2g}}$ or $A_{PL}/A_{E_{2g}}$ as shown in Figure S11 (Supporting Information). Our measurements further exhibit that variations in experimental conditions, such as objective magnification and grating grooves, only affect $(A_{D1} + A_{PL})/A_{E_{2g}}$ by less than 15 % (see Figure S12, Supporting Information).

Limits of the model are discussed in the following. In Figure 4 and Figure S9 (Supporting Information), we observe saturation or a decrease in PL intensity at high fluence above 1 ion/nm^2 , indicating damage to the crystal structure leading to deteriorating influences on the V_B^- system. The crystal damage is also reflected in the broadening of the E_{2g} mode and PL width in Figure S5 (Supporting Information). This indicates that the model is not suited for 30 keV nitrogen ion fluences higher than 1 ion/nm^2 (=1 × 10^{14} ions/cm^2) and imposes a limit. However, this is specific for this type of irradiation. More general, the model is accurate until the onset of PL intensity saturation and E_{2g} broadening for any type of irradiation. It has to be noted that this approach extracts the defect density implicitly from Equation (2). This introduces some ambiguity when inverting the formula and becomes relevant for high density as seen for the last points in Figure 4d, which are therefore expected to deviate.

For comparison, we calculate $(A_{D1} + A_{PL})/A_{E_{2g}}$ from the spectral data given in ref. [8] (see Figure S13, Supporting Information). The estimated spin density of ≈5.9 × 10^{18} cm^{-3}, obtained using the present method, is indicated by an asterisk in Figure 4d. The reported defect density from EPR measurements is ≈5.4 × 10^{17} cm^{-3}, showing a one-order-of-magnitude difference. We ascribe this discrepancy to differences in defect creation processes. Neutron irradiation is highly boron 10-isotope selective[15] and the irradiation fluence that was used for the sample is considered high. This implies that the irradiation is in a region beyond the limits of our model. Furthermore, we expect neutron irradiation to create primarily boron vacancies over other defects.[50] This selectiveness might have severe influence on the Raman active modes. The 3D nature of the neutron irradiated crystal does also impact the E_{2g} mode that we used for our model. To accurately apply our model to neutron irradiated samples, a similar irradiation study to this work would have to be repeated. This would also enable comparison of our model to the estimation of defect density with EPR. We expect our model to be much more comparable with other types of ion irradiation. The results of the SRIM simulation can only be taken qualitatively, i.e. it does not allow us to estimate the exact number of spin defects. The model that SRIM uses does not account for annealing processes at temperatures above 0 K and assumes uncorrelated ion impacts. This reduces the accuracy when predicting effects of high ion fluences like we used in this work. Furthermore, SRIM can only provide information about neutral boron vacancies and not their charge

state. Our model however works directly with signatures of the negative charge state and therefore gives a direct estimation of V_B^- density.

Based on our findigs, we calculate $(A_{D1} + A_{PL})/A_{E_{2g}}$ from the reported spectra, finding values of ≈165 (Ga-irradiated at 1×10^{15} ions/cm^2)[27] and 20 (He-irradiated at 2×10^{14} ions/cm^2),[28] which correspond to spin defect densities of ≈6.2×10^{18} cm^{-3} and 3.2×10^{17} cm^{-3}, respectively. These values are also indicated by asterisks in Figure 4d.

3. Conclusion

In conclusion, our results demonstrate that the new D1 and D2 Raman modes serve as signature peaks of V_B^- defects in hBN. Using polarized Raman spectroscopy and DFT calculations, we investigated the origin of these modes and their relation to atomic vibrational eigenmodes of defects in hBN. We observed that both the intensity of PL and defect-related Raman modes directly depend on the irradiation fluence. Based on these observations, we established an empirical relation linking the integrated area of the D1, E_{2g} and PL modes to the irradiation fluence. The derived model is universally applicable independent of irradiation type and the only method available for thin hBN flakes. This allows for an easy-to-use all-optical quantification of absolute spin defect density present in hBN, making it an indispensable tool for photonic applications of spin defects in hBN.

4. Experimental Section

Experimental: Raman and PL spectra were measured in backscattering configuration using a commercial micro-Raman system (Horiba LabRAM HR800) at room temperature with a 600 lines mm^{-1} grating (spectral resolution ≈3.00 cm^{-1} per CCD pixel). A 100x objective (Olympus, NA = 0.9) with laser spot size of ≈ 1 µm was used, and the laser power was consistently maintained at ≈1 mW.

Computational Methods: All DFT calculations were performed using the Quantum ESPRESSO package v.7.3,[51,52] employing a plane-wave basis set and norm-conserving pseudopotentials. For the V_B^- defect, we considered different supercell sizes with one missing boron atom each, including a single hBN monolayer (4×4 unit cells/31 atoms, 6×6 unit cells/71 atoms, and 8×8 unit cells/127 atoms) and bulk hBN ($8 \times 8 \times 2$ unit cells/511 atoms with four monolayers). The convergence threshold for atomic position relaxation was set to 10^{-5} Ry/Bohr. To avoid spurious distortions in defect-containing supercells, particularly for smaller systems, all calculations were conducted using the equilibrium lattice constants of pristine hBN. However, we note that fixing the lattice constants in some cases can induce spurious imaginary frequencies in the vibrational spectrum. We find the calculated electronic structure and vibrational modes to be robust with respect to the use of either the PBE exchange-correlation functional[53] within the generalized gradient approximation (GGA) or the local density approximation (LDA). For computational reasons, we use the LDA for the calculation of the Raman coefficients.

The vibrational modes of pristine and defect-containing supercells were computed using density functional perturbation theory (DFPT)[54] as implemented in the PHONON module of Quantum ESPRESSO. The localization of each vibrational mode k was quantified using the inverse participation ratio (IPR),[49,55] defined as:

$$\mathrm{IPR}_k = \frac{1}{\sum_a \left(\sum_i \Delta r_{ai,k}^2\right)^2} \quad (3)$$

where $\Delta r_{ai,k}$ is the normalized displacement vector of atom *a* along direction *i* in phonon mode *k*. Nonresonant Raman coefficients were then calculated based on DFPT results by evaluating the second-order response to a uniform electric field.[47] The computed Raman activities were convoluted with a Lorentzian lineshape of 10 cm^{-1} width.

Supporting Information

Supporting Information is available from the Wiley Online Library or from the author.

Acknowledgements

A.P. and P.K. contributed equally to this work. V.D. acknowledges the support by the European Research Council (ERC) (Grant agreement No. 101055454). A.P., P.K., S.H., and V.D. acknowledges the funding by the lighthouse project IQ-Sense of the Bavarian State Ministry of Science and the Arts as part of the Bavarian Quantum Initiative Munich Quantum Valley (15 02 TG 86). S.H., A.S., and V.D. acknowledge financial support from the Würzburg-Dresden Cluster of Excellence on Complexity and Topology in Quantum Matter ct.qmat (EXC 2147, DFG project ID 390858490). L.S. and I.A. acknowledge the Australian Research Council (CE200100010) and the Asian Office of Aerospace Research and Development (FA2386-20-1-4014) for financial support. T.B. and W.G.S. acknowledge computational resources provided by the Paderborn Center for Parallel Computing (PC^2). The authors would also like to thank the authors of refs. [27, 28] for the valuable discussions and for providing spectral data used in comparison with the analysis.

Open access funding enabled and organized by Projekt DEAL.

Conflict of Interest

The authors declare no conflict of interest.

Data Availability Statement

The data that support the findings of this study are available from the corresponding author upon reasonable request.

Keywords

V_B^-, DFT calculations, hBN, photoluminescence, quantum sensing, Raman spectroscopy, spin defects

Received: July 11, 2025
Revised: October 6, 2025
Published online: October 29, 2025

[1] G. Cassabois, P. Valvin, B. Gil, *Nat. Photonics* **2016**, *10*, 262.
[2] A. Gottscholl, M. Kianinia, V. Soltamov, S. Orlinskii, G. Mamin, C. Bradac, C. Kasper, K. Krambrock, A. Sperlich, M. Toth, I. Aharonovich, V. Dyakonov, *Nat. Mater.* **2020**, *19*, 540.
[3] A. Gottscholl, M. Diez, V. Soltamov, C. Kasper, A. Sperlich, M. Kianinia, C. Bradac, I. Aharonovich, V. Dyakonov, *Sci. Adv.* **2021**, *7*, eabf3630.
[4] N. Chejanovsky, A. Mukherjee, J. Geng, Y.-C. Chen, Y. Kim, A. Denisenko, A. Finkler, T. Taniguchi, K. Watanabe, D. B. R. Dasari, P. Auburger, A. Gali, J. H. Smet, J. Wrachtrup, *Nat. Mater.* **2021**, *20*, 1079.

[5] A. Haykal, R. Tanos, N. Minotto, A. Durand, F. Fabre, J. Li, J. Edgar, V. Ivady, A. Gali, T. Michel, A. Dréau, B. Gil, G. Cassabois, V. Jacques, *Nat. Commun.* **2022**, *13*, 4347.
[6] M. Huang, J. Zhou, D. Chen, H. Lu, N. J. McLaughlin, S. Li, M. Alghamdi, D. Djugba, J. Shi, H. Wang, C. R. Du, *Nat. Commun.* **2022**, *13*, 5369.
[7] R. Rizzato, M. Schalk, S. Mohr, J. C. Hermann, J. P. Leibold, F. Bruckmaier, G. Salvitti, C. Qian, P. Ji, G. V. Astakhov, U. Kentsch, M. Helm, A. V. Stier, J. J. Finley, D. B. Bucher, *Nat. Commun.* **2023**, *14*, 5089.
[8] A. Gottscholl, M. Diez, V. Soltamov, C. Kasper, D. Krauße, A. Sperlich, M. Kianinia, C. Bradac, I. Aharonovich, V. Dyakonov, *Nat. Commun.* **2021**, *12*, 4480.
[9] J. E. Fröch, L. P. Spencer, M. Kianinia, D. D. Totonjian, M. Nguyen, A. Gottscholl, V. Dyakonov, M. Toth, S. Kim, I. Aharonovich, *Nano Lett.* **2021**, *21*, 6549.
[10] C. Qian, V. Villafañe, M. Schalk, G. V. Astakhov, U. Kentsch, M. Helm, P. Soubelet, N. P. Wilson, R. Rizzato, S. Mohr, A. W. Holleitner, D. B. Bucher, A. V. Stier, J. J. Finley, *Nano Lett.* **2022**, *22*, 5137.
[11] J. S. Moon, B. Whitefield, L. Spencer, M. Kianinia, M. Hennessey, M. Toth, W. B. Jeon, J.-H. Kim, I. Aharonovich, *Adv. Opt. Mater.* **2024**, *12*, 2401987.
[12] J. Comtet, B. Grosjean, E. Glushkov, A. Avsar, K. Watanabe, T. Taniguchi, R. Vuilleumier, M.-L. Bocquet, A. Radenovic, *Nat. Nanotechnol.* **2020**, *15*, 598.
[13] J. Comtet, A. Rayabharam, E. Glushkov, M. Zhang, A. Avsar, K. Watanabe, T. Taniguchi, N. R. Aluru, A. Radenovic, *Sci. Adv.* **2021**, *7*, eabg8568.
[14] M. Kianinia, S. White, J. E. Fröch, C. Bradac, I. Aharonovich, *ACS Photonics* **2020**, *7*, 2147.
[15] J. Li, E. R. Glaser, C. Elias, G. Ye, D. Evans, L. Xue, S. Liu, G. Cassabois, B. Gil, P. Valvin, T. Pelini, A. L. Yeats, R. He, J. H. Edger, *Chem. Mater.* **2021**, *33*, 9231.
[16] X. Gao, S. Pandey, M. Kianinia, J. Ahn, P. Ju, I. Aharonovich, N. Shivaram, T. Li, *ACS Photonics* **2021**, *8*, 994.
[17] F. F. Murzakhanov, B. V. Yavkin, G. V. Mamin, S. B. Orlinskii, I. E. Mumdzhi, I. N. Gracheva, B. F. Gabbasov, A. N. Smirnov, V. Y. Davydov, V. A. Soltamov, *Nanomaterials* **2021**, *11*, 1373.
[18] W. Liu, N.-J. Guo, S. Yu, Y. Meng, Z.-P. Li, Y.-Z. Yang, Z.-A. Wang, X.-D. Zeng, L.-K. Xie, Q. Li, J.-F. Wang, J.-S. Xu, Y.-T. Wang, J.-S. Tang, C.-F. Li, G.-C. Guo, *Mater. Quantum Technol.* **2022**, *2*, 032002.
[19] F. Tuinstra, J. L. Koenig, *J. Chem. Phys.* **1970**, *53*, 1126.
[20] A. C. Ferrari, D. M. Basko, *Nat. Nanotechnol.* **2013**, *8*, 235.
[21] A. C. Ferrari, J. Robertson, *Phys. Rev. B* **2000**, *61*, 14095.
[22] L. Cançado, K. Takai, T. Enoki, M. Endo, Y. Kim, H. Mizusaki, A. Jorio, L. Coelho, R. Magalhães-Paniago, M. Pimenta, *Appl. Phys. Lett.* **2006**, *88*, 163106.
[23] G. A. Zickler, B. Smarsly, N. Gierlinger, H. Peterlik, O. Paris, *Carbon* **2006**, *44*, 3239.
[24] L. Cançado, A. Jorio, M. Pimenta, *Phys. Rev. B* **2007**, *76*, 064304.
[25] M. M. Lucchese, F. Stavale, E. H. M. Ferreira, C. Vilani, M. V. d. O. Moutinho, R. B. Capaz, C. A. Achete, A. Jorio, *Carbon* **2010**, *48*, 1592.
[26] L. G. Cançado, A. Jorio, E. M. Ferreira, F. Stavale, C. A. Achete, R. B. Capaz, M. d. O. Moutinho, A. Lombardo, T. Kulmala, A. C. Ferrari, *Nano Lett.* **2011**, *11*, 3190.
[27] G. Venturi, S. Chiodini, N. Melchioni, E. Janzen, J. H. Edgar, C. Ronning, A. Ambrosio, *Laser Photonics Rev.* **2024**, 2300973.
[28] F. Ren, Y. Wu, Z. Xu, *J. Lumin.* **2023**, *261*, 119911.
[29] A. Carbone, I. D. Breev, J. Figueiredo, S. Kretschmer, L. Geilen, A. Ben Mhenni, J. Arceri, A. V. Krasheninnikov, M. Wubs, A. W. Holleitner, A. Huck, C. Kast, N. Stenger, *Phys. Rev. Mater.* **2025**, *9*, 056203.
[30] C. Cholsuk, A. Cakan, V. Deckert, S. Suwanna, T. Vogl, *arXiv preprint* **2025**, arXiv:2502.21118.
[31] C. Linderälv, W. Wieczorek, P. Erhart, *Phys. Rev. B* **2021**, *103*, 115421.
[32] T. Vuong, S. Liu, A. Van der Lee, R. Cuscó, L. Artús, T. Michel, P. Valvin, J. Edgar, G. Cassabois, B. Gil, *Nat. Mater.* **2018**, *17*, 152.
[33] E. Janzen, H. Schutte, J. Plo, A. Rousseau, T. Michel, W. Desrat, P. Valvin, V. Jacques, G. Cassabois, B. Gil, J. H. Edgar, *Adv. Mater.* **2024**, *36*, 2306033.
[34] N. Mendelson, D. Chugh, J. R. Reimers, T. S. Cheng, A. Gottscholl, H. Long, C. J. Mellor, A. Zettl, V. Dyakonov, P. H. Beton, S. V. Novikov, C. Jagadish, H. H. Tan, M. J. Ford, M. Toth, C. Bradac, I. Aharonovich, *Nat. Mater.* **2021**, *20*, 321.
[35] M. Koperski, D. Vaclavkova, K. Watanabe, T. Taniguchi, K. S. Novoselov, M. Potemski, *Proc. Natl. Acad. Sci. U. S. A.* **2020**, *117*, 13214.
[36] T. Werninghaus, J. Hahn, F. Richter, D. Zahn, *Appl. Phys. Lett.* **1997**, *70*, 958.
[37] S. Reich, A. Ferrari, R. Arenal, A. Loiseau, I. Bello, J. Robertson, *Phys. Rev. B* **2005**, *71*, 205201.
[38] K. Sasaki, T. Taniguchi, K. Kobayashi, *Appl. Phys. Express* **2023**, *16*, 095003.
[39] S.-Y. Zhang, K. Xu, X.-K. Zhao, Z.-Y. Shao, N. Wan, *Cryst. Growth Des.* **2019**, *19*, 6252.
[40] H. Liu, N. Mendelson, I. H. Abidi, S. Li, Z. Liu, Y. Cai, K. Zhang, J. You, M. Tamtaji, H. Wong, Y. Ding, G. Chen, I. Aharonovich, Z. Luo, *ACS Appl. Mater. Interfaces.* **2022**, *14*, 3189.
[41] X.-L. Liu, X. Zhang, M.-L. Lin, P.-H. Tan, *Chin. Phys. B* **2017**, *26*, 067802.
[42] C. Cong, T. Yu, H. Wang, *ACS Nano* **2010**, *4*, 3175.
[43] Y. Liu, Y.-F. Zhang, S. Jin, S.-P. Li, M.-M. Yang, X.-R. Kong, W. Dang, X.-L. Li, R.-D. Cong, *Opt. Express* **2021**, *29*, 32818.
[44] M.-M. Yang, Y. Liu, R.-D. Cong, Y. Zhang, Y.-F. Zhang, L. Tan, X.-W. Hu, C.-L. Wu, Y.-L. Liu, W. Dang, X.-Y. Liu, X.-H. Zhao, B.-L. Liang, W. Yu, X.-L. Li, *ACS Appl. Nano Mater.* **2023**, *6*, 11299.
[45] M. Hulman, M. Sojkovaá, K. Végsoś, N. Mrkyvkova, J. Hagara, P. Hutár, P. Kotrusz, J. Hudec, K. Tokár, E. Majkova, P. Siffalovic, *J. Phys. Chem. C* **2019**, *123*, 29468.
[46] A. Gale, D. Scognamiglio, I. Zhigulin, B. Whitefield, M. Kianinia, I. Aharonovich, M. Toth, *Nano Lett.* **2023**, *23*, 6141.
[47] M. Lazzeri, F. Mauri, *Phys. Rev. Lett.* **2003**, *90*, 036401.
[48] A. A. Maradudin, *Rep. Prog. Phys.* **1965**, *28*, 331.
[49] A. Alkauskas, B. Buckley, D. Awschalom, C. Van de Walle, *New J. Phys.* **2014**, *16*, 073026.
[50] G. F. Knoll, *Radiation Detection and Measurement*, 4th ed, Wiley, Hoboken, NJ **2010**.
[51] P. Giannozzi, S. Baroni, N. Bonini, M. Calandra, R. Car, C. Cavazzoni, D. Ceresoli, G. L Chiarotti, M. Cococcioni, I. Dabo, A. D. Corso, S. d. Gironcoli, S. Fabris, G. Fratesi, R. Gebauer, U. Gerstmann, C. Gougoussis, A. Kokalj, M. Lazzeri, L. Martin-Samos, N. Marzari, F. Mauri, R. Mazzarello, S. Paolini, A. Pasquarello, L. Paulatto, C. Sbraccia, S. Scandolo, G. Sclauzero, A. P Seitsonen, et al., *J. Condens. Matter Phys.* **2009**, *21*, 395502.
[52] P. Giannozzi, O. Andreussi, T. Brumme, O. Bunau, M. B. Nardelli, M. Calandra, R. Car, C. Cavazzoni, D. Ceresoli, M. Cococcioni, N. Colonna, I. Carnimeo, A. Dal Corso, S. de Gironcoli, P. Delugas, R. A. DiStasio Jr, A. Ferretti, A. Floris, G. Fratesi, G. Fugallo, R. Gebauer, U. Gerstmann, F. Giustino, T. Gorni, J. Jia, M. Kawamura, H.-Y. Ko, A. Kokalj, E. Küçükbenli, M. Lazzeri, et al., *J. Chem. Phys.* **2017**, *29*, 465901.
[53] J. P. Perdew, K. Burke, M. Ernzerhof, *Phys. Rev. Lett.* **1996**, *77*, 3865.
[54] S. Baroni, S. De Gironcoli, A. Dal Corso, P. Giannozzi, *Rev. Mod. Phys.* **2001**, *73*, 515.
[55] R. J. Bell, P. Dean, D. C. Hibbins-Butler, *J. Phys. C: Solid State Phys.* **1970**, *3*, 2111.